

Disorder-Induced Coherence Enables Control of Wave Transport

Israel Kurtz^{1,2}, Yiming Huang^{1,2,3}, Zhou Shi^{1,2,4}, and Azriel Z. Genack^{1,2}

¹*Department of Physics, Queens College of the City University of New York, Flushing, New York 11367, USA*

²*Physics Program, The Graduate Center of the City University of New York, New York New York, 10016, USA*

³*Jinhua No.1 High School, Zhejiang, 321000, China*

⁴*Lightera Labs, 19 School House Road, Somerset, New Jersey 08873, USA*

Illuminating disordered samples with waveforms matched to transmission-matrix eigenchannels produces transmission ranging from complete to vanishing with strong variations in internal energy density, enabling the control of wave propagation for applications in imaging and communications. The origin of these departures from diffusive transport has remained a puzzle since phase coherence is rapidly lost due to scattering. We show here that coherence among waveguide modes grows with sample depth, shaping flux, energy density, and velocity in transmission eigenchannels throughout the sample.

Introduction — When a monochromatic classical wave, such as light or sound, impinges upon a static disordered medium, the wave is scrambled to produce a complex speckle pattern of flux. Analogously, the wave function of electronic quasiparticles is randomized in space but remains temporally coherent when a constant voltage is applied across a mesoscopic conductor. Electronic mesoscopic samples bridge the atomic scale, characterized by elastic scattering, and the macroscopic scale, where inelastic phonon scattering destroys temporal coherence. This regime is realized in micron-sized conductors at ultralow temperatures [1–3]. A full account of both classical and quantum wave transport through stationary random media is embedded within the transmission matrix (TM), t , which relates the flux or current amplitudes in the incident and outgoing transverse modes [4–9].

The TM is experimentally accessible for classical waves [10–18] and provides a theoretical framework for electronic transport [1,4–8,19–22]. Its eigenchannels produce striking variations in transmission, from complete [16,23] to vanishing [24–26], and in internal energy density [27–32]. This opens new avenues for communications, imaging, sensing, and energy delivery [17,33–37]. Although scattering destroys coherence between incident and internal waveguide modes, we show that phase coherence builds among the modes within the medium and governs the departures from diffusive transport in the flux, energy density, and velocity throughout the sample. Interference among contributions to a given eigenchannel seeded by incident modes is either constructive or destructive depending on whether the flux in the eigenchannel is larger or smaller than the average. The balance among incident modal weights and the growth of coherence with depth, while internal modal flux amplitudes diminish, determines the modal

composition of each eigenchannel throughout the sample. This establishes a foundation for controlling transport in complex media.

The optical TM is measured by modifying an incident laser beam profile with a spatial light modulator (SLM) and coherently detecting the transmitted field by overlapping it with a portion of the incident laser on a CCD detector [12]. This approach has made it possible to focus light through random media and to excite transmission eigenchannels (TEs). The optical [14], microwave [13], and acoustic [16] TM can also be measured by translating the source and detector.

In contrast to measurements of classical waves, it is not possible to measure the TM in electronic conductors, since the source and sink of the current are thermal reservoirs. The underlying phase coherence in electronic transport can be inferred only from measurements of conductance fluctuations in a single mesoscopic sample [2,38,3,39,22]. Remarkably, the analytical power of the TM first emerged in theoretical studies of the scaling and statistics of the electronic conductance [4–6,40].

As first recognized by Landauer, quantum transport can be captured by its classical analogue: the dimensionless conductance, $g=G/(e^2/h)$, is equivalent to the transmittance, T , such that $g = T$ [20,21,41]. The transmittance is the sum of transmission coefficients between the N incident and outgoing propagating waveguide modes (WGMs). In waveguide or wire geometries, $T = \sum_{s,m}^N |t_{ms}|^2 = \text{Tr}(tt^\dagger)$, where the elements of the TM, t_{ms} , are the flux amplitudes between the

st incident and the m th outgoing WGMs [21]. Equivalently, the transmittance can be expressed as the sum of the N eigenvalues of tt^\dagger , $T = \sum_{n=1}^N \tau_n$.

Dorokhov showed that the scaling of electronic conductance in ensembles of statistically equivalent mesoscopic wires can be understood in terms of distinct localization lengths associated with each of the N TEs, beyond which the corresponding eigenvalue τ_n decays exponentially with wire length [4,42]. For diffusive waves ($g > 1$), the distribution of transmission eigenvalues is bimodal: roughly g of the eigenvalues have a transmission greater than $\frac{g}{N} \sim \frac{1}{e}$, while most others transmit only weakly [4–6,8].

The statistics of quantum transport were profoundly advanced by linking the statistics of transmission eigenvalues in disordered conductors [4–7] to those of the eigenvalues of the Hamiltonian describing complex nuclei, which are revealed in nuclear scattering experiments [43–45]. This framework captures the universal features of probability density functions (PDFs) of transmission eigenvalues but does not explicitly include the phase coherence that, as shown here, governs departures from the particle-diffusion picture.

Beyond their transmission eigenvalues, TEs also possess distinct average velocities, v_n , which link the flux, τ_n , to the output energy density, $u_n(L)$, through the relation, $\tau_n = u_n(L)v_n$ [46]. The eigenchannel velocities v_n are defined in the Supplementary Materials section in terms of weighted averages over WGM velocities v_m , consistent with the requirement that the density of states for a fixed average dielectric constant be independent of disorder. The eigenchannel

velocities have been characterized statistically at the input and output surfaces [46], but their behavior within the sample has not previously been reported.

TEs are obtained from the singular value decomposition (SVD) of the TM, $t = U\Lambda V^\dagger$, where V and U are unitary matrices with elements v_{sn} and u_{mn} that give the amplitude of the s th WGM of the n th TE at the input and output, respectively [8,17]. The diagonal matrix Λ contains the singular values $\sqrt{\tau_n}$. The WGMs are indexed in order of descending phase velocity v_m , and the TEs are ordered by descending transmission τ_n .

The flux and energy density of TEs at sample surfaces [10,12–17] and within random media [27,28,47,30,32,31] have been examined intensively in recent years, as their broad dynamic range enables control of transmission and energy deposition in complex natural and engineered systems. Yet the origin of the coherence underlying the striking departures of τ_n , $u_n(z)$, and v_n from diffusive predictions has remained obscure, since the coherence of incident modes is rapidly destroyed by scattering. Our microwave measurements and Green's-function simulations reveal that despite rapid randomization of the flux matrix $t(z)$ with depth, coherence re-forms and strengthens with depth among the incident-mode contributions to each eigenchannel. The flux matrix connects incident flux to the sum of the forward- and backward-propagating flux at each cross section of the sample.

Earlier work introduced and measured the deposition matrix in two-dimensional disordered optical waveguides open to the third dimension. The SVD at each depth was used to determine the maximum energy deliverable to any cross section [31,32]. The deposition matrix is

mathematically equivalent to the flux matrix and is likewise obtained from the field matrix [48]. However, while this earlier work retrieved the eigenchannels of the deposition matrix at each depth z , we focus on the flux excited throughout the sample in TEs found from the SVD of the transmission matrix $t(L)$ at the sample output. The TEs can be exploited to control transmission and energy deposition in three-dimensional random media, even when there is no access to the internal field.

Methods — In our experiment, the TM of a copper tube supporting $N = 64$ WGMs randomly filled with dielectric scatterers was obtained from field transmission coefficients between source and receiver antennas using a vector network analyzer (VNA) [13]. The antennas were scanned over a grid of points on the input and output surfaces, as illustrated in Fig. 1(a). Further details of the sample, apparatus, experimental procedures, and data analysis are provided in the Supplementary Materials section.

To investigate the evolution of coherence within the sample, we performed recursive Green's-function simulations [49,50] of the flux matrix at varying depths z in rectangular samples composed of square elements with dielectric constants randomly drawn between 0.7 and 1.3. Each element has a side length $a = \lambda/2\pi$, where λ is the wavelength. Results are reported for a sample of width $W = 26a$ which supports $N = 8$ propagating channels. For a length $L = 300a$, the dimensionless conductance is $g = 2.96$, while for $L = 1000a$, $g = 1.1$. In individual disordered configurations, the WGMs of the empty waveguide do not coincide with the channels of the random waveguide. This leads to fluctuations in the net computed flux in individual configuration. (Supplementary Materials, Fig. S2). However, these random fluctuations cancel

upon averaging over independent configurations, so that the average of the net flux is constant throughout the sample in all TEs (Fig. 5(c)). Details of the simulations are given in the Supplementary Materials.

To identify the factors that determine the modal flux distribution in each TE throughout the sample and to relate these to the corresponding energy density, we decompose the flux at each depth into forward- and backward-propagating components. This is done by evaluating t_{ms} at two adjacent cross sections, z and $z + a$, and assuming that the change in t_{ms} between them arises solely from the phase factor associated with free propagation of the WGM, $e^{\pm i\omega a/v_m}$ (Supplementary Materials). This assumption is justified because $a = \lambda/2\pi \ll \ell$, where the scattering mean free path is $\ell = 133a$. The procedure used to calculate the scattering mean free path [51] is described in the Supplementary Materials.

Results and discussion —

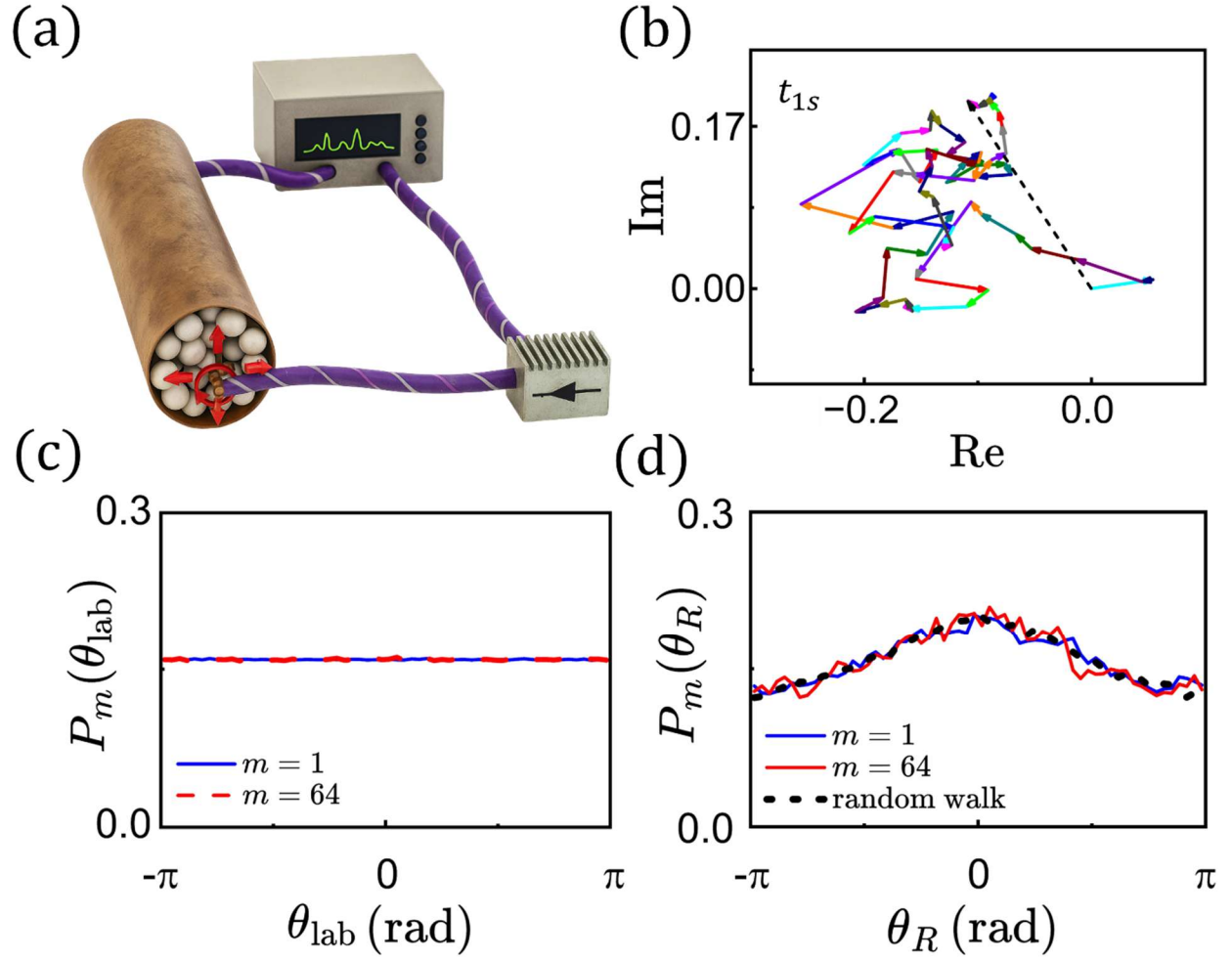


FIG. 1. Microwave measurements of the transmission matrix. (a) Schematic diagram of experimental setup. Spectra of the microwave TM are measured using a VNA and amplifier. (b) Colored arrows indicate TM elements t_{1s} , linking the s th incident WGM to the transmitted $m = 1$ WGM, while the dashed black arrow shows the resultant flux amplitude $t_1 = \sum_{s=1}^{N=64} t_{1s}$ for a single random sample at 14.8497 GHz. (c) PDFs of the phases in the laboratory frame of the $s = 1 \dots N$ components of t_{ms} for $m = 1$ and $m = N = 64$ flux amplitudes in 23 configurations and 801 frequencies for a sample of length $L = 23$ cm. The uniform distributions indicate complete phase randomization. (d) PDFs of the phases in (c) computed relative to their respective resultants, showing the narrowing that arises from alignment with the local resultant.

The flux-matrix elements t_{1s} at a single frequency for one random configuration are represented in Fig. 1(b) as complex vectors (colored arrows), whose orientations with respect to the x-axis indicate their phases relative to each incident WGM s , and whose lengths correspond to $|t_{1s}|$. The resultant, $t_1 = \sum_{s=1}^{64} t_{1s}$, is the vector sum shown by the dashed black arrow. The PDFs of the phase of t_{ms} across frequencies and configurations in the laboratory frame, $P_m(\theta_{\text{lab}})$, are shown in Fig. 1(c) for $m = 1$ and $m = 64$. The flat distributions indicate that the phases of t_{ms} are fully randomized.

The resultant t_1 in the laboratory frame, shown in Fig. 1(b), is larger than any individual vector because it represents a two-dimensional random walk, whose average displacement $\langle t_1 \rangle$ scales as the square root of the number of summed random contributions, $\sqrt{N} = 8$. This scaling reflects the statistical properties of an uncorrelated ensemble of random vectors.

Figure 1(d) shows the PDFs of the phases of t_{1s} relative to the local resultant t_1 , denoted θ_R . The peak that appears in this distribution is consistent with complete phase randomization; it simply reflects that, by construction, the steps of each random walk are aligned with their respective resultants. This interpretation is confirmed by the close agreement between the measured PDFs (blue and red curves) and the simulated distribution (black dashed curve) obtained for 64 randomly oriented vectors.

In contrast, when the sample is excited in a TE, coherence emerges in the sum

$$f_{mn} = \sum_{s=1}^N t_{ms} v_{sn}$$

of individual contributions from each the N incident modes to the m th transmitted WGM in the n th TE.

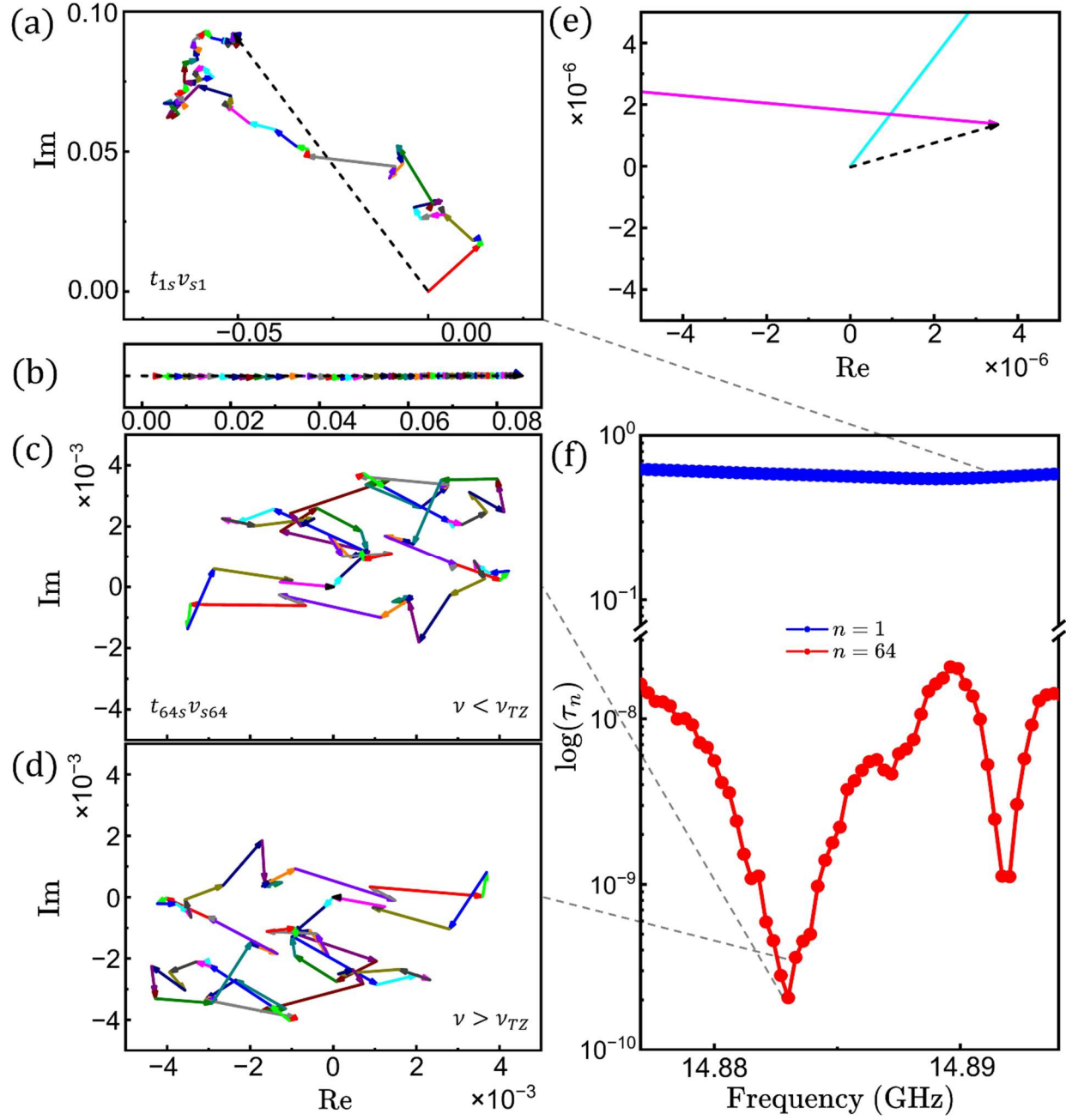


FIG. 2. Measurements of scattering-enhanced coherence in high- and low-transmission TE modes. (a) Vector diagram of the $N = 64$ components, $t_{1s}v_{s1}$, (coloured arrows), and their resultant, $f_{11} = \sum_{s=1}^{N=64} t_{1s}v_{s1}$ (dashed black arrow), which is the amplitude of the flux transmitted in the $m = 1$ WGM of the $n = 1$ TE. Similar constructive interference occurs for all values of m when $n = 1$.

(b) Average of the flux amplitudes $t_{1s}v_{s1}$ over three random samples and 801 frequencies for a sample of length $L = 40$ cm. The resultant is taken to point along the positive x-direction in each configuration. The components interfere constructively. (c)-(e) The vector sum $f_{6464} = \sum_{s=1}^{N=64} t_{64s}v_{s64}$ for the $m = n = N = 64$ WGM at a frequency ν just before (c) and just after (d) a frequency ν_{TZ} at which the transmission vanishes. The contributions to the flux $t_{64s}v_{s64}$ interfere destructively so that the resultant, R , cannot be seen in (c), but appears in (e) when the scale is expanded by a factor of 10^3 . Similar destructive interference occurs for all values of m when $n = 64$. Each component in (c) is seen in (d) to undergo a 180° phase rotation about the origin without noticeable change in magnitude when the frequency is tuned through a TZ at ν_{TZ} . (f) The spectrum of transmission eigenvalues for the highest TE $n = 1$, in a frequency range including (a), and the lowest TE $n = N = 64$, in a frequency range including the TZ in (c)-(e).

The magnitude of the corresponding flux amplitude $|f_{mn}|$ is either enhanced or suppressed depending on whether τ_n lies above or below the mean transmission g/N , as shown in Fig. 2. Constructive interference in a single configuration at one frequency is seen in the formation of $f_{11}(z = L)$ (Fig. 2(a)), where the ratio of coherent to the incoherent flux,

$$\kappa_{mn} = \frac{|\sum_s t_{ms}v_{sn}|^2}{\sum_s |t_{ms}v_{sn}|^2},$$

is found to be $\kappa_{11} = 4.16$. The average coherence factor κ_{11} over the measured configurations is 4.09, compared with unity in the absence of coherence. The average of $f_{11} = \sum_s t_{1s}v_{s1}$, computed with the x-axis in each configuration and frequency aligned along the resultant, reveals

the strong alignment of the individual modal contributions with the resultant (Fig. 2(b)).

Simulations over a large ensemble of random configurations confirm this behavior, showing that the average components of $t_{1s}v_{sn}$ perpendicular to the resultant vanish (Supplementary Fig. S1).

By contrast, interference is nearly perfectly destructive for f_{m64} near a transmission zero (TZ) [24] (Figs. 2(c),(d)). The 64 complex contributions $t_{64s}v_{s64}$ that sum to f_{6464} at frequencies just below and just above the TZ are shown in Figs. 2(c),(d). Across the zero, all flux amplitudes rotate by 180° about the origin. Although the resultant is not visible at the scale of Figs. 2(c),(d), it becomes apparent when the data are magnified by a factor of 10³ (Fig. 2(e)). Similar modal correlations are observed across all TEs.

A segment of the spectra of the highest and lowest transmission eigenvalues, τ_1 and τ_{64} , for this configuration (Fig. 2(f)) reveals a drop in transmission of τ_{64} relative to τ_1 by more than nine orders of magnitude. This level lies over seven orders of magnitude below the noise floor in the measurement of the TM, arising primarily from thermal drift during the 40-hour acquisition time [25].

The source of this apparent imperviousness to noise is evident in Figs. 2(c)-(e). Although the magnitude of the coherent sum of the 64 modal contributions, $t_{64s}v_{s64}$, forming f_{6464} is small, the average magnitude of each term, $|t_{64} v_{s6} |$, is comparable to that of the corresponding terms $t_{1s}v_{s1}$ shown in Fig. 2(a), which contribute to f_{11} . Thus, the small values of τ_{64} arise not from individual vectors of low amplitude, but from their nearly perfect destructive interference in the

coherent sum. The values of $|f_{mn}|^2$ for all m and n are obtained from the simulations described below and shown at the sample output in Fig 3(c) to differ by less than a factor of two.

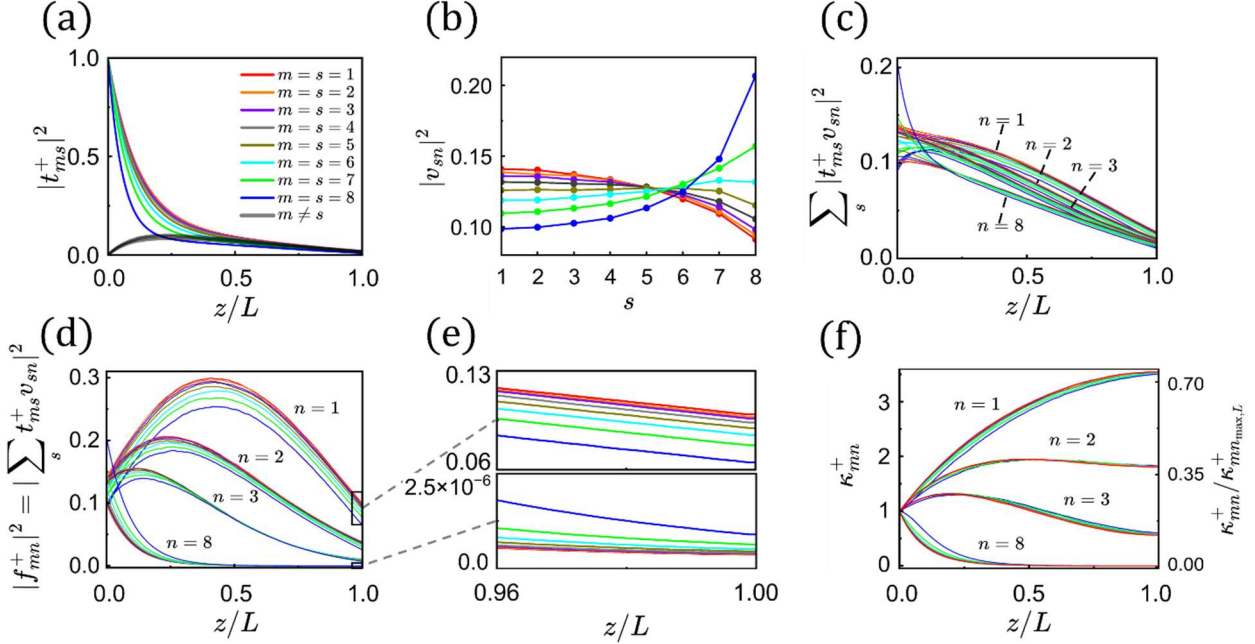


FIG. 3. Buildup of coherence in TE modes with increasing depth into random media. Simulations are carried out on an ensemble of 7.15×10^5 random samples with width $W = 26a$, length $L = 1000a$, disorder strength $\Delta\epsilon = 0.3$, and dimensionless conductance $g \approx 1.1$, at a frequency supporting $N = 8$ propagating channels. (a) The squared amplitudes of the elements of the forward-propagating flux matrix, $|t_m^+|^2$, showing the flux in the m th WGM seeded by the s th incident WGM. As the wave is scattered by the medium, the flux in input modes s is redistributed randomly into modes m . (b) The squared amplitudes of the elements v_{sn} , representing the input waveform of eigenchannel n as a linear combination of incident modes s . Lower velocity WGMs s are progressively weighted more heavily for lower TE modes n . (c) The

incoherent sum of flux seeded by incident WGMs of the $n = 1, 2, 3, 8$ TEs, $\sum_{s=1}^{N=64} |t_{ms}^+ v_{sn}|^2$, decreases both with v_m and with n . The incoherent flux decays with depth and falls most strongly for slow WGMs. (d) The forward flux, given by the coherent sum $|f_{mn}^+|^2 = |\sum_{s=1}^{N=6} t_{ms}^+ v_{sn}|^2$, of the $n = 1, 2, 3, 8$ TEs is strongly differentiated by eigenchannel index n . (e) For high-transmission TEs (n large), higher-velocity WGMs contribute more strongly to the flux, whereas for lower-transmission TEs the trend reverses. This inversion of modal participation underlies the decrease in eigenchannel velocity with smaller τ_n . (f) The degree of constructive interference κ_{mn}^+ , which quantifies the ratio of coherent to incoherent flux shown in (d) and (c). In the highest TE, $\kappa_{mn}^+(L)$ surpasses 70% of $\kappa_{mn_{\max},L}^+$, the maximum degree of constructive interference if all components of coherent flux are perfectly in phase at the sample output.

The squared magnitudes of the two factors in the flux amplitude $t_{ms}^+(z)v_{sn}$, namely $|t_{ms}^+(z)|^2$ and $|v_{sn}|^2$, are shown in Figs. 3(a) and 3(b). The smaller diagonal elements for slower modes in Fig. 3(a) arise from their shorter penetration depths, $v_m \ell/c$, which represent the distance a mode travels during one mean free scattering time, ℓ/c . The off-diagonal elements increase within roughly one mean free path before decaying along with the diagonal elements. The squared amplitudes of the elements of the unitary matrix V , $|v_{sn}|^2$ (Fig. 3(b)), represent the weights of the WGMs in each incident TE. These weights shift progressively toward lower-velocity WGMs as the TE index n increases, leading to a corresponding decrease in the eigenchannel velocity v_n with increasing n [46]. The incoherent sums of flux contributions seeded by incident WGMs, $\sum_{s=1}^{N=8} |t_{ms}^+(z)v_{sn}|^2$, for TEs with $n = 1, 2, 3, 8$ are shown in Fig. 3(c). Beyond a depth of one mean free path, these sums decrease both with depth and with WGM velocity, as shown in Fig. 3(c).

This behavior contrasts with the physical directional flux resulting from the coherent superposition of the directional WGM flux amplitudes within each TE, $f_{mn}^{\pm} = \sum_{s=1}^{N=8} t_{ms}^{\pm}(z)v_{sn}$. The forward flux $|f_{mn}^+|^2$ is shown in Fig. 3(d). For TEs with higher-than-average transmission ($\tau_n > g/N$), the average of the forward-going modal flux, $|f_{mn}^+(z)|^2$ initially increases with depth for all WGMs (Fig. 3(d)). Within these high-transmission channels, the flux also rises systematically with increasing WGM velocity v_m , which corresponds to decreasing modal index m (Figs. 3(d),(e)). In contrast, for TEs with lower-than-average transmission ($\tau_n < g/N$), the modal flux decreases with depth (Fig. 3(d)) and falls with increasing WGM velocity v_m (Figs. 3(d),(e)). The ratio of coherent to incoherent flux in the forward-propagating wave, κ_{mn}^+ , increases when τ_n lies above and decreases when it lies below the ensemble average (Fig. 3(f)). In the highest-transmission eigenchannel, $\kappa_{mn}^+(L)$ exceeds 70% of $\kappa_{mn_{\max,L}}^+ = (\sum_{s=1}^{N=64} |t_{ms}^+(L)v_{sn}|)^2 / \sum_{s=1}^{N=64} |t_{ms}^+(L)v_{sn}|^2$, which is the degree of constructive interference if the components of coherent flux are perfectly in phase. The degree of destructive interference is greatest near transmission zeros [24,25] (Figs. 2(c)–(e)). Figure 3 shows that the magnitude of the forward-going flux in each mode of every eigenchannel, at all depths, $|f_{mn}^+(z)|^2$, is governed by three factors: the squared magnitude of the corresponding transmission-matrix element, $|t_{ms}^+(z)|^2$; the input modal weight, $|v_{sn}|^2$; and the degree of coherence among WGM contributions to each TE, $\kappa_{mn}^+(z)$.

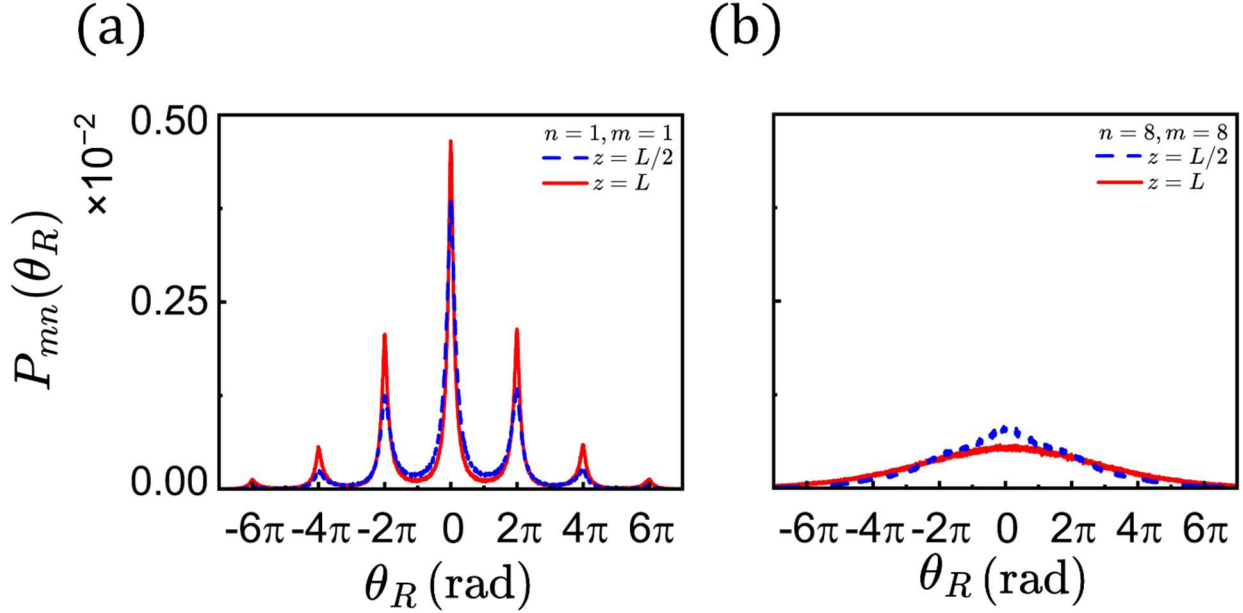


FIG. 4. Narrowing and broadening of angular distribution of flux amplitudes relative to the resultant in highest and lowest TEs. Simulations of 3.12×10^5 random samples performed under the same conditions as in Fig. 3. (a) PDFs of the cumulative phases of the flux amplitudes seeded by the eight incident WGMs forming the $m = 1$ WGM in the $n = 1$ TE, computed relative to the resultant phase in each configuration, at depths $L/2$ and L . The corresponding experimental result at the sample output is shown in Fig. 2(a). With increasing depth, the flux amplitudes align progressively with the resultant, indicating the buildup of coherence. (b) In contrast, the PDF of the cumulative phases of the flux components in the $n = m = 8$ WGM broaden with depth, reflecting the increasingly destructive interference in the lowest TEs.

The degree of mutual coherence is revealed in simulations through the PDF of the cumulative phase of flux amplitudes $t_{ms}^+ v_{sn}$, relative to the resultant in each configuration, $P(\theta_R)$, as shown in Fig. 4. The cumulative phase is found by tracking the phase variation with depth in each configuration. For $n = 1, m=1$, $P(\theta_R)$ is sharply peaked around the resultant, with the peak

becoming more pronounced with increasing depth, indicating the growth of coherence among the vectors (Fig. 4(a)). Secondary peaks in $P(\theta_R)$ at $\theta_R = 2n\pi$ reflect the tendency of the vectors of complex flux amplitude to realign even after becoming oppositely aligned at shallower depths. By contrast, for the $m = 8$ mode of the $n = 8$ TE, $P(\theta_R)$ broadens with depth as interference becomes increasingly destructive (Fig. 4(b)).

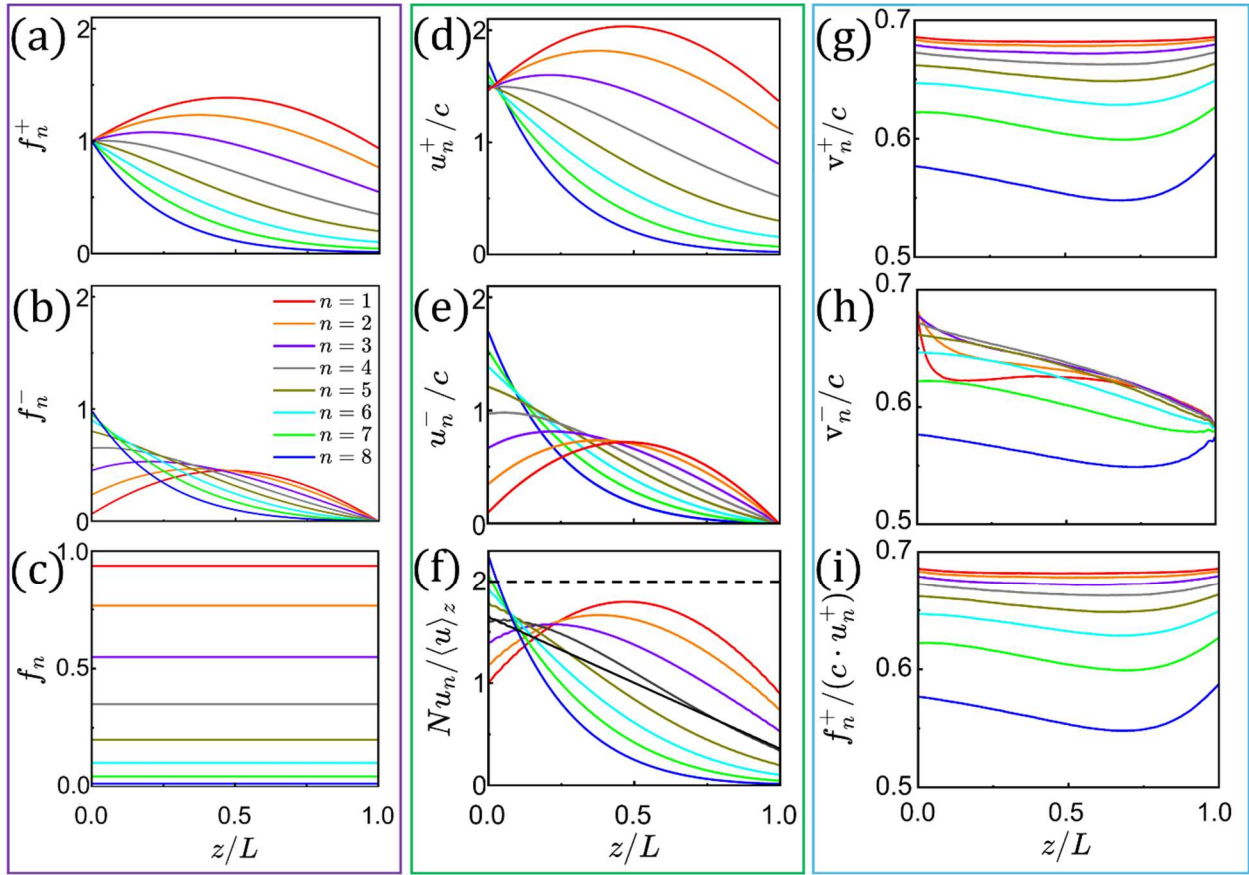


FIG. 5. Eigenchannel flux, energy density, and velocity. Simulations for an ensemble of 5.5×10^4 random samples with the same disorder and width as in Figs. 3 and 4, but with shorter length $L = 300a$ and higher conductance $g \approx 2.96$. (a)-(h) Right- and left-propagating fluxes, energy densities, and velocities for all transmission eigenchannels. The net flux, given by the

difference between right- and left-propagating waves, remains constant throughout the sample and equals the transmission eigenvalue (c). The ensemble-averaged sum of counter-propagating energy densities decreases linearly with depth, as expected for diffusive transport. (f) The total energy density excited by unit flux incident from both sides, which represents each eigenchannel's contribution to the density of states, remains constant with depth (dashed black line). (g),(h) Eigenchannel velocity $v_n^\pm(z)$ exhibits a characteristic dip to a minimum within the sample and returns to its input value at the output surface for both right- and left-propagating waves. **i**, The ratio $f_n^+(z)/u_n^+(z)$ equals $v_n^+(z)$, confirming the relation $f_n^+(z) = u_n^+(z)v_n^+(z)$.

While the contributions of all incident channels to each WGM within a TE add coherently, the modal fluxes of different WGMs combine incoherently to yield the directional fluxes, $f_n^\pm(z) = \sum_{m=1}^N |f_{mn}^\pm(z)|^2$. At the output surface, $f_n^+(L) = \tau_n$ and $f_n^-(L) = 0$. The distinction between coherent interference within modes and incoherent summation across modes underlies the flux, energy density, and velocity profiles shown in Fig. 5.

The forward and backward propagating fluxes, energy densities, and velocities, as well as the relationships among them, for all eigenchannels in samples with the same disorder and width as in Figs. 3 and 4, but with a shorter length $L = 300a$ and correspondingly higher conductance ($g \approx 2.96$), are shown in Figs. 5(a),(b),(d),(e),(g),(h). The net flux, given by the difference between the right- and left-propagating waves in each TE, remains constant throughout the sample and equals the transmission eigenvalue, $f_n^+(z) - f_n^-(z) = \tau_n$ (Fig. 5(c)), while the average energy density decreases linearly with depth, as expected for diffusing waves. The total energy

density excited by unit flux incident from both sides of the sample in each TE, which is proportional to the density of states, is constant (dashed black line in Fig. 5(f)). The eigenchannel velocity shows a characteristic dip to a minimum within each eigenchannel before rising at the output to match its value at the input surface, for both waves propagating to the right (Fig. 5(g)) and to the left (Fig. 5(h)). The ratio $f_n^+(z)/u_n^+(z)$, shown in Fig. 5(i), is identical to $v_n^+(z)$, in accordance with the relation

$$f_n^+(z) = u_n^+(z)v_n^+(z).$$

Conclusions — Although the TM maps the incoming singular vectors onto the outgoing ones, theoretical investigations have largely characterized transport and the extent of control via the scalar transmission eigenvalues of tt^\dagger , τ_n . By analogy with the eigenvalues of the Hamiltonian of large nuclei [44], the statistics of τ_n have been related to the positions of parallel lines of charge embedded in a compensating background, with their spacing determined by mutual repulsion [7,8]. Here we have shown that, most directly, it is the coherence among the modal flux amplitudes of the singular vectors that fundamentally underlies the wide range of transmission and energy density in TEs. This mutual coherence governs the degree of constructive or destructive interference throughout the sample, thereby determining the spatial profiles of flux, energy density, and velocity within each WGM of every eigenchannel. Remarkably, the degree of coherence among different eigenchannels changes little over the length scale of the scattering mean free path.

The ratio of transmission among waveguide modes within TEs evolves systematically with eigenchannel index (Fig. 3(d)). In the highest-transmission channel ($n = 1$), WGMs with higher velocities carry greater flux. This differential in mode transmission diminishes and reaches a minimum for the TE whose transmission is closest to the mean, g/N . For lower-transmission TEs, the trend reverses, and modes with lower velocities transmit more strongly. This accounts for the observed decrease in eigenchannel velocity with decreasing transmission, as seen in Fig. 5(g). This work reveals an unexpected degree of mutual coherence among WGMs generated by scattering in random media. This coherence fixes the relative contributions of the modal fluxes both within each TE and across different TEs throughout the sample, leading to eigenchannel bands with closely spaced subbands in $f_{mn}^\pm(z)$ and to a reversal in their ordering as the TE index n increases.

The resulting correlations are most pronounced in TEs for which $\tau_n \approx 1$, where interference among all WGMs within each eigenchannel is nearly fully constructive, and at transmission zeros, where interference is fully destructive and the flux in all WGMs vanishes simultaneously as either the energy density or velocity of the TE approaches zero [25]. Because it is the coherence among the modal flux amplitudes, rather than their individual magnitudes, that determines the transmission eigenvalues, TEs can be accurately measured and their properties exploited. For example, the predicted square root singularity in the frequency spacing between transmission zeros [24] should be observable and could be utilized for highly sensitive measurements of configuration change. While we have mapped the consequences of this coherence, the microscopic origin of its growth with depth across the $2N^2$ forward- and backward-propagating modal contributions $f_{mn}^\pm(z)$ remains to be established. Clarifying this

mechanism would advance the informed use of the TM for selective control of WGMs and TEs, with implications for communications, imaging, sensing, and targeted energy delivery in complex media.

Acknowledgements — The authors thank Nipun Koshy for valuable discussions. This work is supported by the National Science Foundation (US) under NSF-BSF Award No. 2211646 (AZG).

Data availability — The data used in the current study are available from the corresponding author on reasonable request.

References

- [1] B. L. Altshuler, P. A. Lee, and W. R. Webb, *Mesoscopic Phenomena in Solids* (Elsevier, 2012).
- [2] Klitzing, K. V., Dorda, G. & Pepper, M. New method for high-accuracy determination of the fine-structure constant based on quantized Hall resistance. *Phys. Rev. Lett.* **45**, 494–497 (1980).
- [3] R. A. Webb, S. Washburn, C. P. Umbach, and R. B. Laibowitz, Observation of h/e Aharonov-Bohm oscillations in normal-metal rings, *Phys Rev Lett* **54**, 25 (1985).
- [4] O. N. Dorokhov, Transmission coefficient and the localization length of an electron in N bound disordered chains, *Soviet Journal of Experimental and Theoretical Physics Letters* **36**, 318 (1982).
- [5] Y. Imry, Active transmission channels and universal conductance fluctuations, *Europhys. Lett.* **1**, 5 (1986).

[6] P. A. Mello, P. Pereyra, and N. Kumar, Macroscopic approach to multichannel disordered conductors, *Annals of Physics* **181**, 2 (1988).

[7] Stone, A. D., Mello, P. A., Muttalib, K. A. & Pichard, J.-L. Random matrix theory and maximum entropy models for disordered conductors. in *Mesoscopic Phenomena in Solids* 369–448 (North-Holland, Amsterdam, 1991).

[8] C. W. J. Beenakker, Random-matrix theory of quantum transport, *Rev. Mod. Phys.* **69**, 3 (1997).

[9] M. Buttiker, Coherent and sequential tunneling in series barriers, *IBM Journal of Research and Development* **32**, 1 (1988).

[10] M. C. W. van Rossum and T. M. Nieuwenhuizen, Multiple scattering of classical waves: microscopy, mesoscopy, and diffusion, *Rev. Mod. Phys.* **71**, 313 (1999).

[11] I. M. Vellekoop and A. P. Mosk, Focusing coherent light through opaque strongly scattering media, *Opt. Lett.*, **OL 32**, 16 (2007).

[12] Popoff, S. M., Lerosey, G., Carminati, R., Fink, M., Boccara, A. C., Gigan, S. Measuring the transmission matrix in optics: an approach to the study and control of light propagation in disordered media. *Phys. Rev. Lett.* **104**, 100601 (2010).

[13] Shi, Z. & Genack, A. Z. Transmission eigenvalues and the bare conductance in the crossover to Anderson localization. *Phys. Rev. Lett.* **108**, 043901 (2012).

[14] Yu, H., Hillman, T. R., Choi, W., Lee J. O., Feld, M. S., Dasari, R. R., Park, Y. K. Measuring large optical transmission matrices of disordered media. *Phys. Rev. Lett.* **111**, (2013).

[15] S. M. Popoff, A. Goetschy, S. F. Liew, A. D. Stone, and H. Cao, Coherent control of total transmission of light through disordered media, *Phys. Rev. Lett.* **112**, 13 (2014).

- [16] B. Gérardin, J. Laurent, A. Derode, C. Prada, and A. Aubry, Full transmission and reflection of waves propagating through a maze of disorder, *Phys. Rev. Lett.* **113**, 17 (2014).
- [17] S. Rotter and S. Gigan, Light fields in complex media: Mesoscopic scattering meets wave control, *Rev. Mod. Phys.* **89**, (2017).
- [18] L. Devaud, B. Rauer, J. Melchard, M. Kühmayer, S. Rotter, and S. Gigan, Speckle engineering through singular value decomposition of the transmission matrix, *Phys. Rev. Lett.* **127**, 9 (2021).
- [19] R. Landauer, Electrical resistance of disordered one-dimensional lattices, *The Philosophical Magazine: A Journal of Theoretical Experimental and Applied Physics* **21**, 172 (1970).
- [20] Economou, E. N. & Soukoulis, C. M. Static conductance and scaling theory of localization in one dimension. *Phys. Rev. Lett.* **46**, 618–621 (1981).
- [21] D. S. Fisher, P. A. Lee, C. W. Hsu, and A. D. Stone, Relation between conductivity and transmission matrix, *Phys. Rev. B* **23**, 6851 (1981).
- [22] M. Büttiker, Y. Imry, R. Landauer, and S. Pinhas, Generalized many-channel conductance formula with application to small rings, *Phys. Rev. B* **31**, 10 (1985).
- [23] Sweeney, W. R., Hsu, C. W., & Stone, A. D. Theory of reflectionless scattering modes. *Phys. Rev. A* **102**, (2020).
- [24] Y. Kang and A. Z. Genack, Transmission zeros with topological symmetry in complex systems, *Phys. Rev. B* **103**, 10 (2021).
- [25] K. Joshi, I. Kurtz, Z. Shi, and A. Z. Genack, Ohm’s law lost and regained: observation and impact of transmission and velocity zeros, *Nat Commun* **15**, 10616 (2024).

[26] Erb, J., Shaibe, N., Calvo, R., Lathrop, D. P., Antonsen, Jr., T. M., Kottos, T., Anlage, S. M. Topology and manipulation of scattering singularities in complex non-Hermitian systems: Two-channel case. *Phys. Rev. Res.* **7**, 023090 (2025).

[27] W. Choi, A. P. Mosk, Q.-H. Park, and W. Choi, Transmission eigenchannels in a disordered medium, *Phys. Rev. B* **83**, 13 (2011).

[28] M. Davy, Z. Shi, J. Park, C. Tian, and A. Z. Genack, Universal structure of transmission eigenchannels inside opaque media, *Nature Communications* **6**, 1 (2015).

[29] Sarma, R., Yamilov, A. G., Petrenko, S., Bromberg, Y. & Cao, H. Control of energy density inside a disordered medium by coupling to open or closed channels. *Phys. Rev. Lett.* **117**, (2016).

[30] Bender, N., Yamilov, A., Yilmaz, H. & Cao, H. Fluctuations and correlations of transmission eigenchannels in diffusive media. *Phys. Rev. Lett.* **125**, 165901 (2020).

[31] Bender, N., Yamilov, A., Goetschy, A., Yilmaz, H., Hsu, C. W., Cao, H. Depth-targeted energy delivery deep inside scattering media. *Nat. Phys.* **18**, 309–315 (2022).

[32] McIntosh, R. Goetschy, A., Bender, N., Yamilov, A., Hsu, C. W., Yilmaz, H., Cao, H. Delivering broadband light deep inside diffusive media. *Nat. Photon.* **18**, 744–750 (2024).

[33] A. P. Mosk, A. Lagendijk, G. Lerosey, and M. Fink, Controlling waves in space and time for imaging and focusing in complex media, *Nature Photon* **6**, 283 (2012).

[34] Bertolotti, J., Van Putten, E. G., Blum, C., Lagendijk, A., Vos W. L., Mosk, A. P. Non-invasive imaging through opaque scattering layers. *Nature* **491**, 232–234 (2012).

[35] Chaigne, T., Katz, O., Boccara, A. C., Fink, M., Bossy, E., Gigan, S. Controlling light in scattering media non-invasively using the photoacoustic transmission matrix. *Nature Photon* **8**, 58–64 (2014).

[36] A. Boniface, J. Dong, and S. Gigan, Non-invasive focusing and imaging in scattering media with a fluorescence-based transmission matrix, *Nat Commun* **11**, 6154 (2020).

[37] Bender, N., Goetschy, A., Hsu, C. W., Yilmaz, H., Palacios, P. J., Yamilov, A., Cao, H. Coherent enhancement of optical remission in diffusive media. *Proceedings of the National Academy of Sciences* **119**, e2207089119 (2022).

[38] B. L. Altshuler, D. Khmel'nitzkii, A. I. Larkin, and P. A. Lee, Magnetoresistance and Hall effect in a disordered two-dimensional electron gas, *Phys. Rev. B* **22**, 11 (1980).

[39] Lee, P. A. & Stone, A. D. Universal conductance fluctuations in metals. *Phys. Rev. Lett.* **55**, 1622–1625 (1985).

[40] J.-L. Pichard, N. Zanon, Y. Imry, and A. Douglas Stone, Theory of random multiplicative transfer matrices and its implications for quantum transport, *J. Phys. France* **51**, 7 (1990).

[41] R. Landauer, Electrical resistance of disordered one-dimensional lattices, *The Philosophical Magazine: A Journal of Theoretical Experimental and Applied Physics* **21**, 863 (1970).

[42] O. N. Dorokhov, On the coexistence of localized and extended electronic states in the metallic phase, *Solid State Communications* **51**, 381 (1984).

[43] E. P. Wigner, On the behavior of cross sections near thresholds, *Phys. Rev.* **73**, 9 (1948).

[44] Dyson, F. J. Statistical theory of the energy levels of complex systems. I. *J. Math. Phys.* **3**, 140–156 (1962).

[45] M. L. Mehta, *Random Matrices* (Elsevier, 2004).

[46] A. Z. Genack, Y. Huang, A. Maor, and Z. Shi, Velocities of transmission eigenchannels and diffusion, *Nat Commun* **15**, 2606 (2024).

[47] Sarma, R., Yamilov, A. G., Petrenko, S., Bromberg, Y., Cao, H. Control of energy density inside a disordered medium by coupling to open or closed channels. *Phys. Rev. Lett.* **117**, (2016).

[48] X. Cheng and A. Z. Genack, Focusing and energy deposition inside random media, *Opt. Lett.*, **OL 39**, 6324 (2014).

[49] H. U. Baranger, D. P. DiVincenzo, R. A. Jalabert, and A. D. Stone, Classical and quantum ballistic-transport anomalies in microjunctions, *Phys. Rev. B* **44**, 19 (1991).

[50] G. Metalidis, Electronic transport in mesoscopic systems, (2007).

[51] Z. Shi and A. Z. Genack, Diffusion in translucent media, *Nat Commun* **9**, 1 (2018).

[52] A. A. Chabanov, M. Stoytchev, and A. Z. Genack, Statistical signatures of photon localization, *Nature* **404**, 850 (2000).

Supplementary Materials

Israel Kurtz^{1,2}, Yiming Huang^{1,2,3}, Zhou Shi^{1,2,4}, and Azriel Z. Genack^{1,2}

¹*Department of Physics, Queens College of the City University of New York, Flushing, New York 11367, USA*

²*Physics Program, The Graduate Center of the City University of New York, New York New York, 10016, USA*

³*Jinhua No.1 High School, Zhejiang, 321000, China*

⁴*Lightera Labs, 19 School House Road, Somerset, New Jersey 08873, USA*

Figures

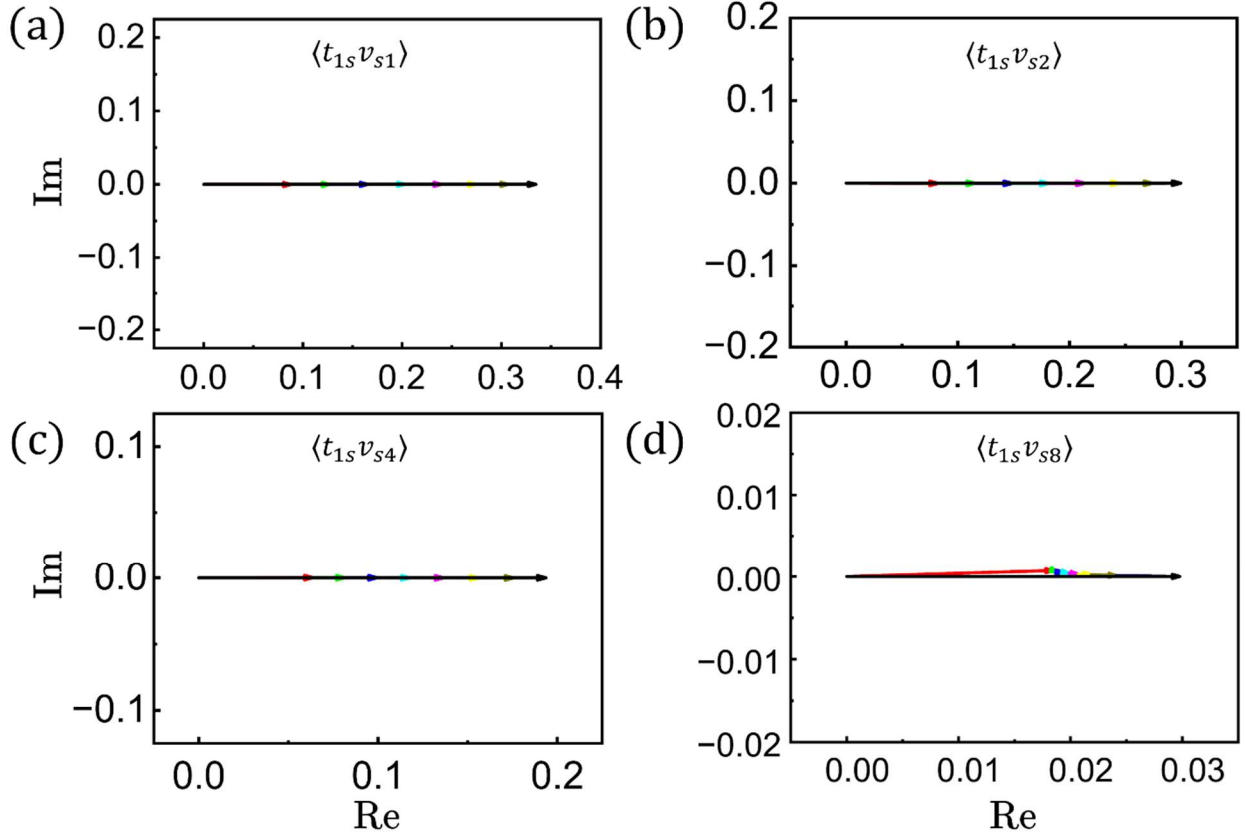


FIG. S1. Ensemble average flux amplitude components. Simulations of 1.2×10^6 random samples with width $W = 26a$, length $L = 1000a$, disorder strength $\Delta\epsilon = 0.3$, and dimensionless conductance $g \approx 2.96$, at a frequency supporting $N = 8$ propagating channels. (a)-(d) For transmission eigenchannels 1,2,4, and 8, and for the waveguide mode $m = 1$, the ensemble-averaged vector sum $\langle \sum_s t_{ms} v_{sn} \rangle$ is shown, with the resultant oriented along the horizontal axis in each configuration. The mean resultant amplitude decreases systematically with eigenchannel index, reflecting the increase of destructive interference in lower-transmission channels.

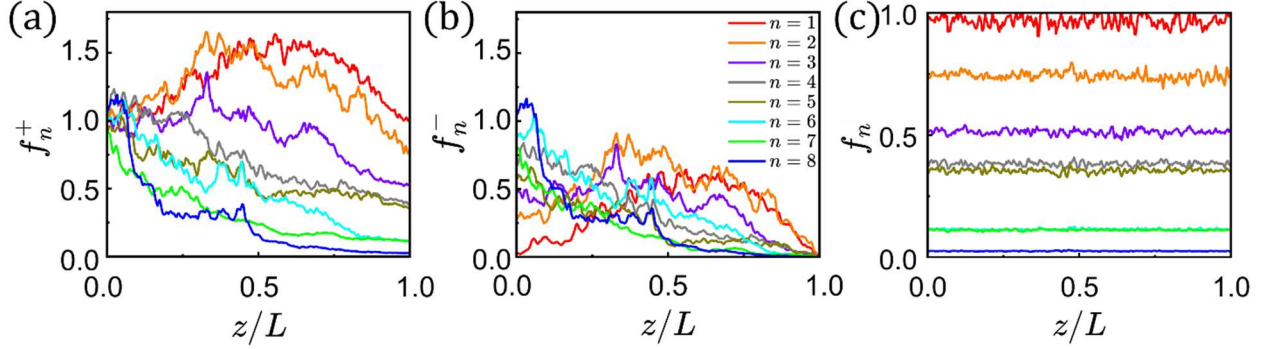


FIG. S2. Flux in a single random sample. Simulations for a single random sample with the same disorder and width as in Supplementary Fig. 1, but with shorter length $L = 300a$ and higher conductance $g \approx 2.96$. Average flux per eigenchannel versus depth: (a) right-propagating, (b) left-propagating, and (c) net flux. Net flux fluctuates with depth in individual realizations of the sample but is constant when averaged over configurations.

Methods

Experimental setup — Spectra of the TM of random dielectric waveguides were measured using the microwave setup shown schematically in Fig. 1(a) [1]. Each sample consisted of randomly distributed alumina spheres, with a diameter of 0.95 cm and refractive index of 3.14, embedded in Styrofoam shells to achieve an alumina volume fraction of 6.9%. The composite medium was housed within a copper tube of inner diameter 7.3 cm. Measurements were performed on 23 statistically independent realizations of disorder for length $L = 23$ cm and 3 configurations of length $L = 40$ cm with use of a vector network analyzer (VNA) over the frequency range 14.70 – 14.94 GHz. The source and detector antennas were separated from the sample faces by 2 cm-long empty waveguide sections.

The VNA output was amplified to deliver a power of approximately 1 W. For each realization, field transmission spectra were acquired for two perpendicular orientations of the source and detector antennas at all input-output position pairs on a 9 mm \times 9 mm grid of points. The antennas were formed from the central conductors of copper-clad coaxial cables, whose exposed tips were bent at 90° and aligned parallel to the sample surface. Emission and detection were both polarized along the antenna axis. To generate new random configurations, the sample was rotated about its axis and then gently vibrated so that the spheres would be stable over the ≈ 40 hours required to record the full TM for a single configuration.

In a sample without absorption, at a frequency at which transmission in the lowest TE drops to zero, the amplitudes of all WGMs contributing to the flux in the lowest TE must fall to zero. In addition, the phases of the components of the flux matrix rotate by 180° at the frequency immediately following the TZ, as compared to their phases at the frequency preceding it, as in Fig. 2(c),(d). However, the experimental samples contain absorption that varies both with space and with frequency of incident radiation, which distorts both of these phenomena. To compensate for absorption within the sample, the measured transmission spectra were first multiplied by a Gaussian envelope centered at each frequency point and then Fourier transformed into the time domain. The time-domain signal was multiplied by an exponentially increasing factor $e^{\gamma t}$. The applied gain, γ , compensates for the decaying field amplitude caused by absorption. The signal was truncated once the noise level approached the signal amplitude to suppress the influence of noise at later times. The signal was then transformed back into the frequency domain. This yielded a modified spectrum in which the artificial gain compensates statistically for absorption

losses in the medium [2,3]. Following this correction, the PDF of intensity matched that expected for a sample without dissipation.

Recursive Green's function — We simulate electromagnetic wave propagation in rectangular samples built from a square lattice where each cell has side length $a = \frac{\lambda}{2\pi}$ and a dielectric constant ϵ drawn from a rectangular distribution centred at $[1 - \Delta\epsilon, 1 + \Delta\epsilon]$. The sample is attached to semi-infinite leads on the left and right, while the upper and lower edges are perfectly reflecting. This setup is equivalent to having a medium that extends uniformly and without bound in the direction perpendicular to the rectangle's plane. The frequency at which simulations are carried out is $\sim 66\%$ of the spectral distance between the crossovers from 7 channels to 8 and from 8 channels to 9.

To compute the fields, we use the recursive Green's function (RGF) technique [4,5], evaluating the response in the k th column for a source placed at the sample's left edge. The structure is divided into K columns of width a , indexed as $1, 2, \dots, k, \dots, K$. Starting from the surface Green's function of the left lead, we add columns sequentially from left to right, attaching each new column k to the subsystem consisting of columns 1 through $k - 1$. The connection between column k and the preceding subsystem is described through the Dyson equation, $G = G_0 + G_0 V G$, where G is the Green's function of the connected block of columns 1 through k , G_0 is the Green's function matrix for the subsystem $1 \dots k - 1$ plus the isolated column k , and V contains the coupling between columns $k - 1$ and k . The final expression,

$$G_{k1} = [1 - G_{kk}^L V_{k,k+1} G_{k+1,k+1}^R V_{k+1,k}]^{-1} G_{k1}^L,$$

yields the Green's functions connecting all columns from 1 through K and provides the basis for computing the field amplitudes and flux throughout the sample.

Flux matrix — Although the elements of the TM show no obvious phase relationship, the amplitudes of WGMs in different TEs vary exponentially. We therefore analyze each WGM component of the TEs at depth z as a superposition of contributions excited by the incident TE. To do this, we use RGF simulations to find the field matrix $e_{ba}(z)$, between the incident field of unit flux at transverse position a and the field within the sample at depth z and transverse position b .

The field matrix is transformed into the basis of waveguide modes

$$\varphi_m = \sqrt{\frac{2}{w}} \sin\left(\frac{m\pi y}{w}\right) e^{i\beta_m z},$$

according to

$$t_{ms}(z) = 2i\sqrt{v_m v_s} \iint_0^W e_{ba}(z) \varphi_m^*(z, y_b) \varphi_s(z, y_a) dy_a dy_b,$$

where v_m and v_s are the group velocities of the m th and s th WGMs.

The transmission matrix t is then decomposed by singular value decomposition (SVD) as $t = U\Lambda V^\dagger$, yielding its singular vectors and singular values.

The flux amplitude in the m th WGM of the n th TE at depth z , is given by $f_{mn}(z) = \sum_s t_{ms}(z) v_{sn}$.

The flux amplitude can be decomposed into the right- and left-propagating coefficients, $f_{mn}^+(z)$ and $f_{mn}^-(z)$, by expressing the flux at z and $z + \Delta z$ as

$$f_{mn}(z) = f_{mn}^+(z) + f_{mn}^-(z)$$

and

$$f_{mn}(z + \Delta z) = f_{mn}^+(z)e^{ik_m \Delta z} + f_{mn}^-(z)e^{-ik_m \Delta z}.$$

The fluxes $f_{mn}(z)$ and $f_{mn}(z + \Delta z)$ are used to determine the coefficients $f_{mn}^+(z)$ and $f_{mn}^-(z)$.

Results are obtained by taking $\Delta z = a$, for which the phase change is appreciable while scattering is minimal.

The right and left propagating fluxes in the n^{th} eigenchannel are

$$f_n^\pm = \sum_m |f_{mn}^\pm|^2.$$

The net flux,

$$f_n = \sum_m (|f_{mn}^+|^2 - |f_{mn}^-|^2),$$

equals the transmission eigenvalue $\tau_n = \lambda_n^2$, where λ_n is the n^{th} singular value of the matrix Λ .

The flux in a single random configuration is not constant at all depths z (Supplementary Fig S2); it is only constant when averaged over an ensemble of such configurations. This reflects the circumstance that the transverse modes are eigenchannels of the uniform medium, not of the random medium.

Eigenchannel energy density and velocity — The right- and left-propagating linear energy density in the n^{th} eigenchannel are

$$u_n^\pm = \sum_m \frac{1}{v_m} |f_{mn}^\pm|^2.$$

The total energy density is

$$u = \sum_{m,n} (|f_{mn}^+| + |f_{mn}^-|)^2.$$

The right- and left-propagating velocities in the n th eigenchannel are the WGM velocities v_m , weighted by the corresponding right- and left-propagating fluxes in each WGM and normalized by the total flux. We define

$$v_n^\pm = \left\langle \frac{1}{v_n^\pm} \right\rangle^{-1} = \frac{\langle \sum_m |f_{mn}^\pm|^2 \rangle}{\langle \sum_m \left(\frac{1}{v_m} |f_{mn}^\pm|^2 \right) \rangle}.$$

The corresponding fluxes satisfy

$$f_n^\pm = u_n^\pm v_n^\pm.$$

The average eigenchannel velocity is

$$v_n = \left\langle \frac{1}{v_n} \right\rangle^{-1} = \frac{\langle \sum_m (|f_{mn}^+ + f_{mn}^-|^2) \rangle}{\langle \sum_m \frac{1}{v_m} (|f_{mn}^+ + f_{mn}^-|^2) \rangle};$$

it follows that $f_n = u_n v_n$. At the sample output, v_n is equal to v_n^+ .

Determination of the Scattering Mean Free Path — The scattering mean free path, ℓ_s , was obtained from simulations of the exponential decay of the coherent flux due to multiple scattering in disordered waveguides [6]. The coherent flux, represented by the ensemble-averaged transmitted field intensity, $|\langle t_{mm} \rangle|^2$, quantifies the portion of the wave that propagates through the medium without losing phase correlation with the incident field. As the sample length L increases, this coherent component decays exponentially, following

$$|\langle t_{mm} \rangle|^2 \propto e^{-L/\ell_s}.$$

Although the rate of decay can differ among input modes, when the decay is plotted as a function of the coherent time delay, L/v_m , where v_m is the modal group velocity, the curves for all modes collapse onto a single exponential function. The associated decay constant defines the scattering mean free time, τ_s , via

$$|\langle t_{mm} \left(\frac{L}{v_m} \right) \rangle|^2 \propto e^{-t/\tau_s}.$$

The scattering mean free path is obtained from

$$\ell_s = c\tau_s.$$

- [1] Shi, Z. & Genack, A. Z. Transmission eigenvalues and the bare conductance in the crossover to Anderson localization. *Phys. Rev. Lett.* **108**, 043901 (2012).
- [2] K. Joshi, I. Kurtz, Z. Shi, and A. Z. Genack, Ohm's law lost and regained: observation and impact of transmission and velocity zeros, *Nat Commun* **15**, 10616 (2024).
- [3] A. A. Chabanov, M. Stoytchev, and A. Z. Genack, Statistical signatures of photon localization, *Nature* **404**, 850 (2000).
- [4] H. U. Baranger, D. P. DiVincenzo, R. A. Jalabert, and A. D. Stone, Classical and quantum ballistic-transport anomalies in microjunctions, *Phys. Rev. B* **44**, 19 (1991).
- [5] G. Metalidis, Electronic transport in mesoscopic systems, (2007).
- [6] Z. Shi and A. Z. Genack, Diffusion in translucent media, *Nat Commun* **9**, 1 (2018).